Particles II

Access the latest eBook →

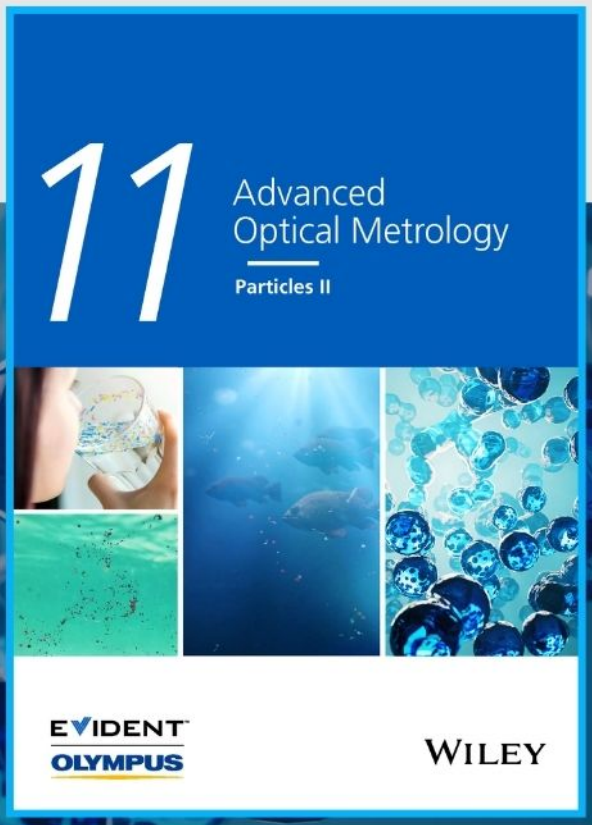

Impact on Biological Systems and the Environment

This eBook is dedicated to the research of Professor David Wertheim.
In collaboration with various groups, Professor Wertheim uses confocal microscopy to analyse the impact of different types of particles on human health and the environment, with a focus on human health-hazardous particles detected with solid-state nuclear track detectors (SSNTD). Download for free, today.

EVIDENT
OLYMPUS

WILEY

ADVANCED MATERIALS
www.advmat.de

Tackling Disorder in γ-Ga_2O_3

Laura E. Ratcliff, Takayoshi Oshima, Felix Nippert, Benjamin M. Janzen, Elias Kluth, Rüdiger Goldhahn, Martin Feneberg, Piero Mazzolini, Oliver Bierwagen, Charlotte Wouters, Musbah Nofal, Martin Albrecht, Jack E. N. Swallow, Leanne A. H. Jones, Pardeep K. Thakur, Tien-Lin Lee, Curran Kalha, Christoph Schlueter, Tim D. Veal, Joel B. Varley, Markus R. Wagner, and Anna Regoutz**

Ga_2O_3 and its polymorphs are attracting increasing attention. The rich structural space of polymorphic oxide systems such as Ga_2O_3 offers potential for electronic structure engineering, which is of particular interest for a range of applications, such as power electronics. γ-Ga_2O_3 presents a particular challenge across synthesis, characterization, and theory due to its inherent disorder and resulting complex structure–electronic-structure relationship. Here, density functional theory is used in combination with a machine-learning approach to screen nearly one million potential structures, thereby developing a robust atomistic model of the γ-phase. Theoretical results are compared with surface and bulk sensitive soft and hard X-ray photoelectron spectroscopy, X-ray absorption spectroscopy, spectroscopic ellipsometry, and photoluminescence excitation spectroscopy experiments representative of the occupied and unoccupied states of γ-Ga_2O_3. The first onset of strong absorption at room temperature is found at 5.1 eV from spectroscopic ellipsometry, which agrees well with the excitation maximum at 5.17 eV obtained by photoluminescence excitation spectroscopy, where the latter shifts to 5.33 eV at 5 K. This work presents a leap forward in the treatment of complex, disordered oxides and is a crucial step toward exploring how their electronic structure can be understood in terms of local coordination and overall structure.

1. Introduction

Gallium oxide is an ultrawide-bandgap (UWBG) semiconductor that promises to extend the capabilities and application limits in areas such as power electronics, solar blind UV photodetectors, gas-sensing devices, and solar cells.[1,2] It is already successfully used in some areas, including phosphors and electroluminescent (EL) devices,[3] solar-blind photodetectors,[4,5] photocatalysis,[6] and power electronics.[7,8] Ga_2O_3 is similar to many other polymorphic oxide systems, such as Al_2O_3, In_2O_3, and Sb_2O_3, in that beyond the thermodynamically stable monoclinic β-phase ($C2/m$) at least four further phases exist. These include the rhombohedral α-Ga_2O_3 ($R\bar{3}c$), cubic γ-Ga_2O_3 ($Fd\bar{3}m$), orthorhombic ε/κ-Ga_2O_3 ($Pna2_1$), and cubic δ-Ga_2O_3 ($Ia\bar{3}$) phases. It should be noted that the existence of the δ-phase is still subject to some discussion and it has been suggested that it may be formed by a mixture of the β- and ε/κ-phases.[9]

L. E. Ratcliff
Department of Materials
Imperial College London
London SW7 2AZ, UK

L. E. Ratcliff
Center for Computational Chemistry
School of Chemistry
University of Bristol
Bristol BS8 1TS, UK
E-mail: laura.ratcliff@bristol.ac.uk

The ORCID identification number(s) for the author(s) of this article can be found under https://doi.org/10.1002/adma.202204217.

[+]Present address: Department of Mathematical, Physical and Computer Sciences, University of Parma, Viale delle Scienze 7/A, Parma 43124, Italy

DOI: 10.1002/adma.202204217

T. Oshima
Department of Electrical and Electronic Engineering
Saga University
Saga 840-8502, Japan

F. Nippert, B. M. Janzen, M. R. Wagner
Technische Universität Berlin
Institute of Solid State Physics
Hardenbergstrasse 36, 10623 Berlin, Germany

E. Kluth, R. Goldhahn, M. Feneberg
Institut für Physik
Otto-von-Guericke-Universität Magdeburg
Universitätsplatz 2, 39106 Magdeburg, Germany

P. Mazzolini,[+] O. Bierwagen
Paul-Drude-Institut für Festkörperelektronik
Leibniz-Institut im Forschungsverbund Berlin e.V.
Hausvogteiplatz 5-7, 10117 Berlin, Germany

C. Wouters, M. Nofal, M. Albrecht
Leibniz-Institut für Kristallzüchtung
Max-Born-Str. 2, 12489 Berlin, Germany

J. E. N. Swallow
Department of Materials
University of Oxford
Parks Road, Oxford OX1 3PH, UK

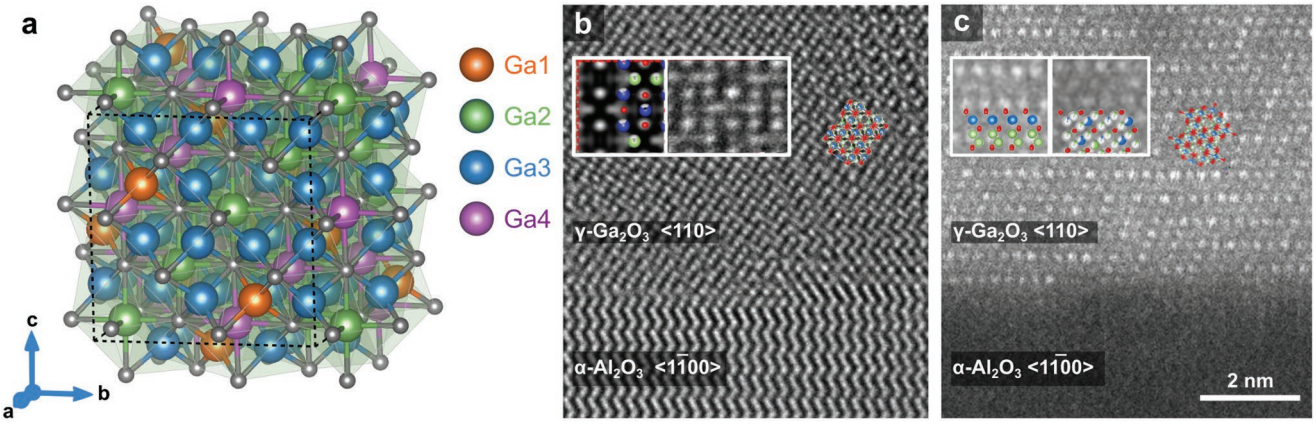

Figure 1. Atomic structure of γ-Ga_2O_3. a) Schematic representation of the crystal structure with inequivalent Ga positions given numbers (1,3) for tetrahedral T_d and (2,4) for octahedral O_h ordination. b,c) Atomic resolution image of γ-Ga_2O_3 crystallized on a sapphire substrate. b) High-resolution phase contrast image along the [110] projection. The inset shows an expanded view as well as an image simulation. The latter is overlaid with an atomic model (red atoms are oxygen, green, and blue are fourfold and sixfold coordinated Ga atoms. c) STEM high-angle annular dark-field image of the same area. The bright atoms correspond to Ga. An atomic model is overlaid to the image. The image pattern fluctuates between a single periodicity and a double periodicity along the (111) planes of the structure. The inset shows details of the microscopy image that correspond to an occupation resembling that of the β-structure in the <132 > projection (double periodicity, left inset) and to an occupation of the γ-structure along the <110 > projection (single periodicity, right inset). Figure 1a was prepared using the VESTA software package.[57]

The existence of γ-Ga_2O_3 was first suspected by Böhm in 1939,[10] and subsequent works by Roy et al. and Pohl led to the conclusion that it has a spinel-type structure similar to γ-Al_2O_3.[11,12] Although these initial observations of the γ-phase took place in the first half of the 20th century, it took until 2013 for detailed structural investigations to be performed by Playford et al. using total neutron diffraction.[9,13] Whilst the analogy to γ-Al_2O_3 still holds in that γ-Ga_2O_3 can be considered to be a cubic, cation-deficient spinel with only partial occupancy of its tetrahedral and octahedral sites, Playford et al. conclusively showed that the distribution of occupied sites results in an inherently disordered structure. **Figure 1**a shows a schematic representation of the crystal structure of γ-Ga_2O_3. In addition to the expected ideal spinel sites, tetrahedral (T_d) 8a (Ga1) and octahedral (O_h) 16d sites (Ga2), T_d 48f (Ga3) and O_h 16c (Ga4) sites are also partially occupied, with a refined tetrahedral to octahedral ratio from Playford et al. of 1:1.35. Furthermore, the local structure of γ-Ga_2O_3 is distorted, with the O_h 16d sites having distinct long and short Ga–O distances and showing the most significant degree of local distortion.

Previous first principles calculations of γ-Ga_2O_3 based on density functional theory (DFT)[14,15] have focused on systematically exploring all possible structures arising due to different combinations of vacant Ga sites, both for pure γ-Ga_2O_3[16] and Mn-doped γ-Ga_2O_3.[17] Similar approaches have been employed for γ-Al_2O_3.[18–20] While the exhaustive search approach has led to some interesting insights regarding the preferred vacancy sites in γ-Ga_2O_3, it is made tractable due to the assumption of a 2-site defective spinel structure. However, the proposed 4-site model of Playford et al. leads to a number of possible configurations that makes such an approach prohibitively expensive. Similarly, the need to impose stoichiometry, combined with the low occupancies for two of the four sites, increases the size of the unit cell needed to effectively define the structure. Other approaches for structure searching and optimization of Ga_2O_3 have been employed, however, these have focused on other phases[21] or 2D structures,[22] while the large number of required calculations in such approaches poses challenges for systems containing many atoms. One way to overcome such size limitations is via the use of interatomic potentials, which have been previously employed to explore a very large number of potential structures for γ-Al_2O_3.[23] However, this relies on the availability of a potential which is accurate enough to distinguish between structures which are close in energy. In a previous study by some of the present authors, a combination of X-ray spectroscopy and theory was successfully used to explore the influence of local Ga coordination on the electronic structure across the α, β, and ε polymorphs.[24] However, the γ-phase was not included at the time as its inherent disorder proved challenging.

The present work significantly extends previous efforts to prepare, characterize, and model γ-Ga_2O_3. A detailed understanding

L. A. H. Jones, T. D. Veal
Stephenson Institute for Renewable Energy and Department of Physics
University of Liverpool
Liverpool L69 7ZF, UK
P. K. Thakur, T.-L. Lee
Diamond Light Source Ltd.
Diamond House
Harwell Science and Innovation Campus
Didcot OX11 0DE, UK
C. Kalha, A. Regoutz
Department of Chemistry
University College London
20 Gordon Street, London WC1H 0AJ, UK
E-mail: a.regoutz@ucl.ac.uk
C. Schlueter
Deutsches Elektronen-Synchrotron DESY
Notkestrasse 85, 22607 Hamburg, Germany
J. B. Varley
Lawrence Livermore National Laboratory
Livermore, CA 94550, USA

of the influence of structural disorder on the electronic structure of γ-Ga_2O_3, including the nature of the occupied and unoccupied states, as well as the bandgap and alignment, is crucial to provide a firm knowledge base for this and other disordered materials, as well as for furthering optimization and implementation across different applications. To achieve this, first principles calculations are combined with a machine-learning (ML) approach to accelerate the screening of possible structures in 160 atom cells. The predicted low energy configurations are shown to provide a good description of the experimental data, whilst clear deviations are found for the higher energy configurations, confirming that these are not a realistic description of the disorder in γ-Ga_2O_3. Soft and hard X-ray photoelectron spectroscopy (XPS and HAXPES) in combination with X-ray absorption spectroscopy (XAS) provide a direct experimental probe for the electronic structure as well as distinguishing between surface and bulk contributions. Complementary spectroscopic ellipsometry and photoluminescence excitation spectroscopy (PLE) results add further information on the bandgap and related transitions.

2. Results

2.1. Atomic-Level Disorder

Whilst the neutron diffraction experiments and analysis by Playford et al.[9,13] provide crucial insights into the disorder present in γ-Ga_2O_3, electron microscopy can probe this on much shorter length scales. Figure 1b shows an atomic resolution phase contrast image of γ-Ga_2O_3 thin films obtained under imaging conditions, where atoms appear as bright dots. The image shows the interface between the sapphire substrate and the crystalline Ga_2O_3 layer along the $\langle 1\bar{1}00 \rangle$ projection of the sapphire substrate. The layer is single crystalline, and the image pattern fits well to that of the γ-phase of Ga_2O_3. A ball and stick model is overlaid to indicate the positions of the oxygen (red) and the octahedrally coordinated (blue) and tetrahedrally coordinated (green) Ga atoms. Image simulations were done considering only partial occupation of the various Ga sites according to the model by Playford et al.[9,13] The best fit between the image pattern and the simulations was obtained for projected sample thickness of 10 nm. The inset shows the simulation with the atoms overlaid and a detail of the microscopy image. Two key observations can be made in this image. While the oxygen sublattice is periodic and characterized by intense bright spots under the imaging conditions used here, translational symmetry in the Ga sublattice is not present and the image pattern fluctuates at the nanometer scale. This indicates a strong local fluctuation in the occupancy of the various Ga sites, as expected for the defective spinel structure. While neutron scattering and X-ray methods are integrating across larger volumes, TEM data, such as those presented here, can resolve these fluctuations on much shorter length scales. In case of phase contrast images such as shown in Figure 1b the TEM sample has a thickness of 3 nm along the viewing direction. The phase shift of the electron wave then scales linearly with the atomic density. Thus density fluctuations can be mapped in the image plane with true atomic resolution integrating the atomic columns along the beam direction. In case of STEM HAADF images (Figure 1c) the thickness of the sample is considerably higher (50 nm), while the in-plane resolution is still at the atomic columns level. This finding is confirmed by scanning transmission electron microscopy images using a high-angle annular dark-field detector (see Figure 1c), where only Ga atoms are visible. As can be seen, the image pattern fluctuates, with the apparent change of the periodicity along the (111) planes between a single periodicity and a double periodicity. The latter corresponds to an occupancy of the Ga sites that is close to the β-phase in its [132] projection, shown in the inset in Figure 1c, while single periodicity corresponds to the γ-structure in the [110] projection. The structures in the projections show a common oxygen lattice with almost identical positions with the γ-phase having a higher number of Ga sites with stochastic occupation. These TEM results provide further evidence of the inherent disorder of both Ga and O in γ-Ga_2O_3, emphasizing the need to build atomistic models that take this aspect of its intrinsic structure into account.

2.2. High-Throughput Structure Screening

The initial random structure generation, PBE-based DFT calculations, and process for augmenting the data set, which are described in Section 4, are summarized in the first two rows of **Figure 2**. The performance of the model coming from the resulting 839 structures and denoted "ML1," is depicted in **Figure 3**a,b. As can be seen, the mean absolute error (MAE) across the validation set converges at around 300 structures in the training set, while the MAE for the largest training set size is 5.9 meV per atom. However, the DFT energies across the 839 structures (depicted in Figure 3e) are spread out across a range of around 0.3 eV per atom, with the majority distributed around the center of that range. Therefore, a more important measure of the success of the model is whether or not it is able to find low energy structures, which are not well represented in the data set.

To this end, an additional 40 000 structures were generated, using the four site probabilities. All structures with a predicted energy lower than E_{ref} + 0.02 eV per atom were calculated, where E_{ref} is the lowest energy seen thus far. The majority of the 45 new structures (69%) were indeed found to have DFT energies within 0.02 eV per atom of E_{ref} (see Table S1, Supporting Information). However, as shown in Figure 3f, a number of structures were 0.1 eV per atom or higher in energy, demonstrating that the initial model did not adequately cover the low energy region of interest. Therefore, the model was refit by splitting the full set of data into 590 (294) training (validation) structures, as summarized in row three of Figure 2.

The performance of the new model, denoted "ML2," is depicted in Figures 3c,d. The convergence with training set size is slower than for ML1, while the MAE for the largest training set size is 7.5 meV per atom, slightly higher than for ML1, but nonetheless reasonable. In order to verify whether or not the new model had improved predictivity for low energy structures, a further 250 000 structures were generated, this time including 10% of structures with explicit two site occupancies. The same energy criterion was used to identify potential low energy structures, that is, $E_{\text{ML2}} - E_{\text{ref}} < 0.02$ eV per atom. As shown in row four of Figure 2, this resulted in an additional 171 structures,

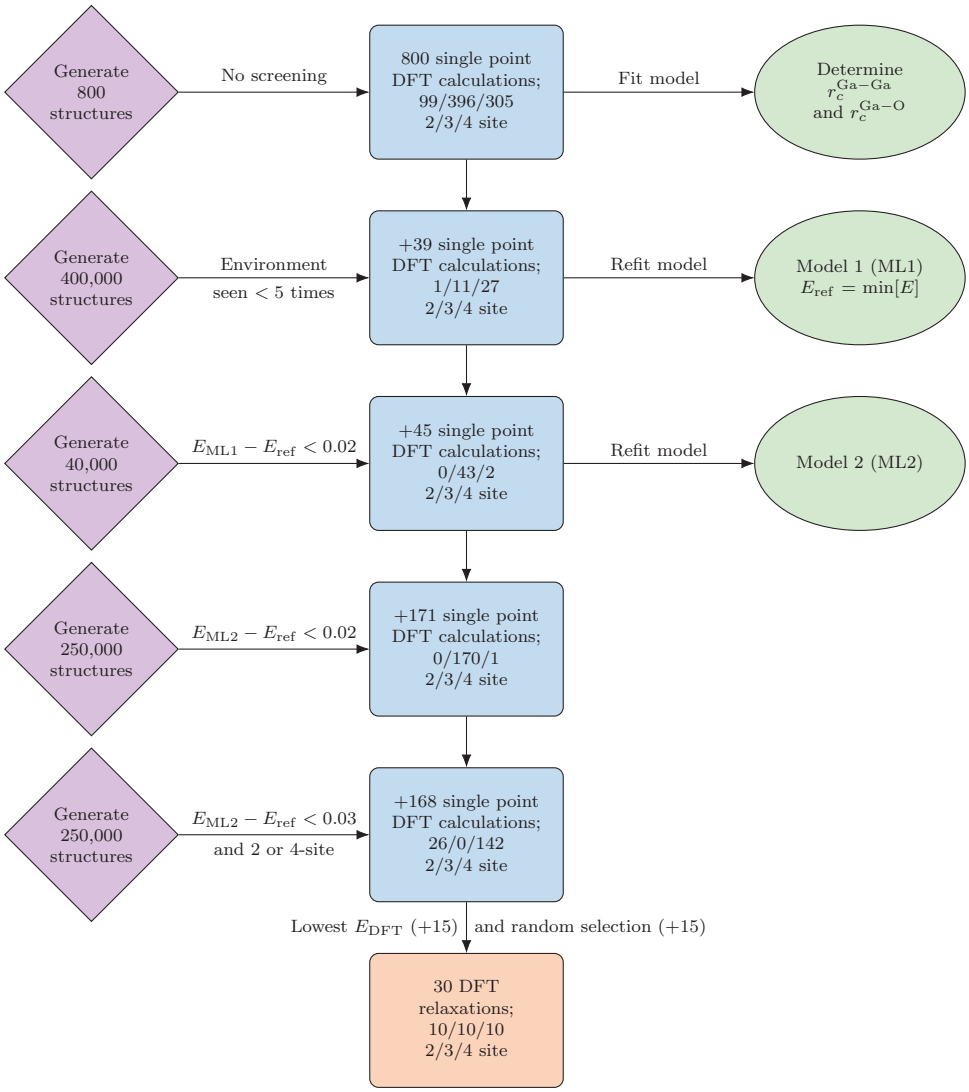

Figure 2. Flowchart summarizing the process for generating, screening and calculating structures, as well as fitting the machine-learning (ML) model. Energy thresholds are in eV per atom.

all but one of which had three of the Ga sites occupied. As can be seen from Figure 3g and Table S1, Supporting Information, the majority of the structures were within the targeted range (79%), with the remainder being only slightly higher in energy. More importantly, there were no high-energy outliers.

As a final step, another 250 000 structures were generated, as in the previous step, however the energy threshold was increased to 0.03 eV per atom, and all 3-site structures were rejected. This resulted in an additional 168 DFT structures, of which 26 (142) had two (four) sites occupied, as summarized in row five of Figure 2. As shown in Figure 3h all of these structures were higher in energy than the lowest identified 3-site structures.

2.3. Atomic Structure

Out of the full set of 1223 DFT-calculated structures, 30 structures were relaxed. The structures were selected first by taking the five lowest energy 2-, 3-, and 4-site structures, respectively. An additional 15 structures were then randomly selected to give a total of ten structures each with two, three and four occupied Ga sites. Particularly for the higher energy structures, some Ga atoms moved considerably during relaxation, and thus the type of Ga site was redetermined for each Ga atom by identifying the closest corresponding Ga site in the pristine structure. The structures were then reclassified by the number of occupied Ga sites. The unrelaxed and relaxed energies, and the site occupancies for the 30 structures are given in Table S2, Supporting Information.

For the unrelaxed structures, the lowest energy structures all have three occupied Ga sites, with the 4-site structures being next lowest in energy, at around 8 meV per atom higher in energy. The 2-site structures are slightly higher in energy. This is further evident in Figure S1, Supporting Information, where the distribution of all unrelaxed energies is given by number of occupied Ga sites. After relaxation, the lower energy structures

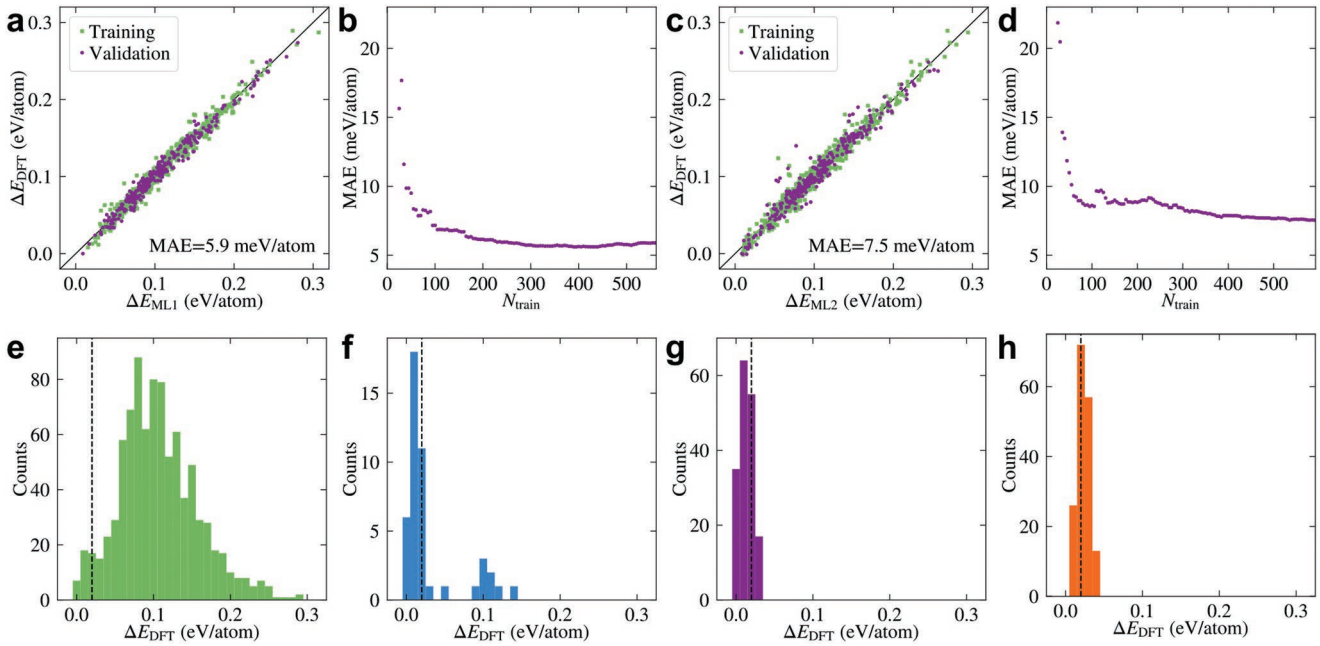

Figure 3. Performance of the different models, including a comparison to the DFT results and ability to predict low energy structures. a,b) The model performance for the initial 800 structures plus those containing rare environments (ML1), while (c) and (d) are for the refitted model, which has an additional 45 predicted low energy structures (ML2). Also shown in (a) and (c) are the mean absolute errors (MAEs) for the largest training set. (e)–(h) show the distribution of PBE-calculated energies for: e) the initial structures plus those containing rare environments, f) structures where the ML1 predicted energy was less than 0.02 eV per atom above the reference energy, g) structures where the ML2 predicted energy was less than 0.02 eV per atom above the reference energy, and h) structures where the ML2 predicted energy was less than 0.03 eV per atom above the reference energy, and for which only 2 or 4 distinct Ga sites were occupied.

remain lower in energy than those selected randomly, but with some rearrangements within the group (see Figure S2, Supporting Information). Notably, the 3- and 4-site relaxed structures are at similar energies, with the lowest energy 3-site structure being less than 1 meV per atom lower in energy than the lowest energy 4-site structure. The 2-site relaxed structures remain slightly higher in energy, but are also closer in energy than before relaxation, with the lowest 2-site being 7 meV per atom higher than the overall lowest energy structure. However, such small energy differences are relatively insignificant given the sensitivity to simulation parameters including the basis set and pseudopotential. Indeed, when comparing relative energies of the relaxed structures calculated using CASTEP with those calculated with BigDFT (depicted in Figure S2, Supporting Information), the ordering changes and the relative energies differ on average by 4.0 meV per atom. Therefore, in the following, structures within 10 meV per atom of the lowest energy structure are grouped together, and are all considered to be low in energy. We note that the energies calculated using HSE after further relaxation differ more significantly from the BigDFT PBE energies, however, despite a smaller range of values, the trend is well preserved (see Figure S2, Supporting Information), and thus unless otherwise stated, relative energies are those calculated with BigDFT. For the randomly selected structures, a considerable number of structures contain Ga atoms which change site following relaxation, while the relative energies also change considerably. As a result, only two randomly selected structures have two occupied Ga sites, both of which are relatively low in energy, while there remain some 3- and 4-site structures which are relatively high in energy.

The lowest energy PBE-relaxed 2-, 3-, and 4-site structures are depicted in **Figure 4**a, where the distortions away from ideal octa- and tetrahedra are clearly visible, as expected based on the neutron diffraction results.[9,13] This is also evident in the smearing of the correlation function (depicted for the lowest energy structure in Figure S3, Supporting Information) and in the spreading out of both Ga and O atoms around their undistorted positions (depicted in Figure S4, Supporting Information for the low energy structures). We note that the structures were further relaxed using HSE for the bandgap calculations, however, this did not have a significant effect on the atomic positions (0.01 Å average displacement). To further investigate the distortions, the Ga–O bond lengths were analysed for all 30 relaxed structures. These were determined by identifying the 4 (6) closest O atoms for each tetrahedral (octahedral) Ga atom, giving rise to the average, maximum and minimum bond lengths for each type of Ga site in a given structure. The results are depicted in Figure 4b. Disorder is present in the bonds associated with all four Ga sites, but to a much greater extent for the O_h sites. The two O_h sites also show a larger difference in average bond lengths—taking the lowest energy 4-site structure (IVA), the average bond lengths are 1.85, 1.99, 1.83, and 2.10 Å for Ga sites 1 to 4, respectively, which are in good agreement with the values from Playford et al.[13] Although the average bond lengths are relatively consistent across all structures, the O_h sites show a large variation for a number of the higher energy structures, with some bond lengths deviating

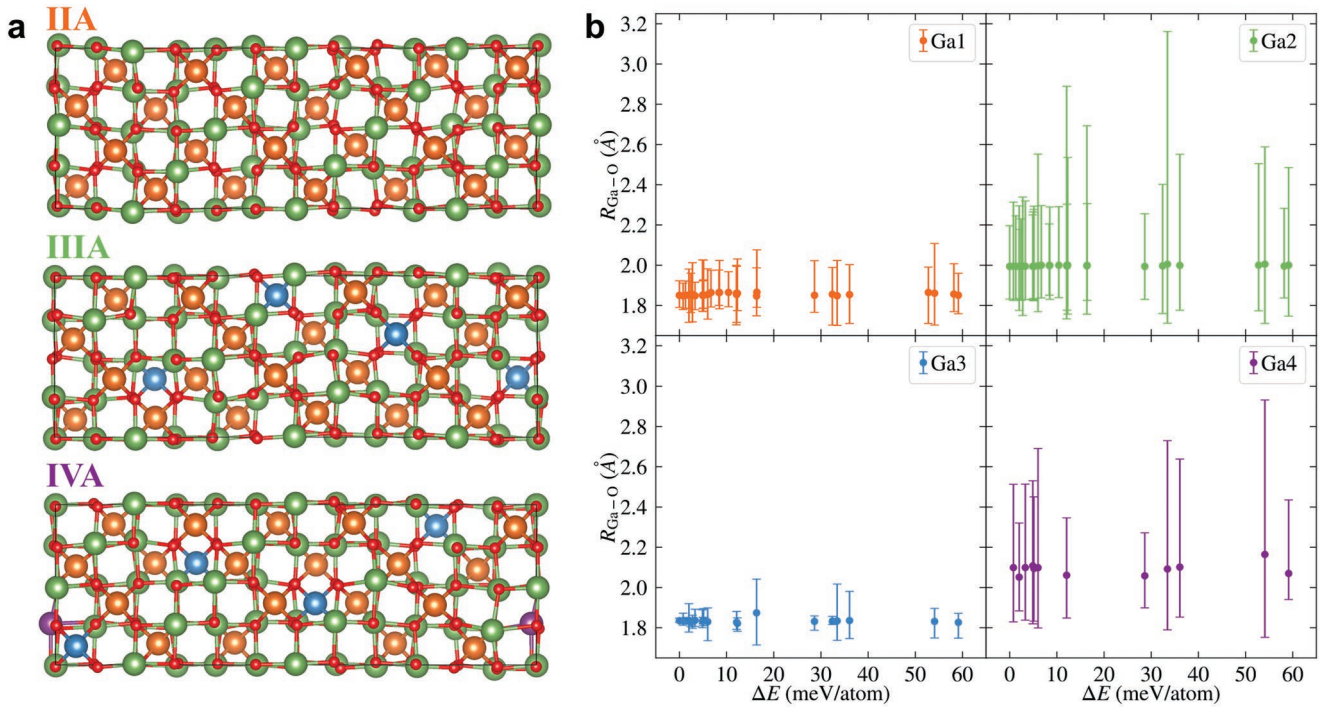

Figure 4. Relaxed structures of γ-Ga_2O_3. a) Lowest energy relaxed 2- (IIA), 3- (IIIA), and 4- (IVA) site structures, with Ga sites 1/2/3/4 depicted in orange/green/blue/purple, and O atoms in red, as viewed along the *b*-axis. b) Ga–O bond lengths for the 30 relaxed structures versus the relative energy of that structure, for each type of Ga site. Shown is both the average bond length (points) and the minimum and maximum bond lengths (error bars) in a given structure. Figure 4a was prepared using the VESTA software package.[57]

significantly from the expected values. Such deviations suggest the presence of unrealistic local environments, in other words these high energy structures are poor representations of the atomic structure of γ-Ga_2O_3.

2.4. Occupied and Unoccupied States

HSE was used to calculate the bandgaps for the 30 relaxed structures (see **Figure 5**a) with a clear trend of lowest energy structures having the largest bandgaps. The bandgap value for the lowest energy structure, which is a 3-site structure, is 4.69 eV, which is smaller than the 4.87 eV bandgap of the β-Ga_2O_3 from HSE calculations.[25] This is in agreement with the narrowing of the bandgap observed in the experimental SXPS and XAS data, which are plotted on a common energy scale for both the γ and β polymorphs in Figure 5b (see Figure S5, Supporting Information for the full range O K-edge XAS spectrum). The 0 eV point of the common energy scale is aligned to the experimental Fermi energy E_F position as determined from the SXPS experiments. In line with our previous results on the other polymorphs, the E_F appears within the bandgap toward the conduction band minimum (CBM), indicating that γ-Ga_2O_3 is nondegenerate n-type. However, due to limitations in the common energy scale alignment, as well as possible small influences from surface band bending, this approach cannot be used to extract reliable bandgap values. Therefore, a combination of spectroscopic ellipsometry and PLE spectroscopy was used to further explore the bandgap experimentally.

The experimentally determined point-by-point fitted dielectric function is shown in Figure 5c. The onset of strong absorption is visible by the increase of ε_2 at an energy of ≈5.1 eV, determined by the characteristic energy of a model dielectric function used to describe the point-by-point result. This value is related to the lowest allowed direct band-to-band transition in the material, but lowered by Coulomb interaction due to excitonic effects. This value is very similar to that of other polymorphs of Ga_2O_3, namely an averaged optical response over x and y directions of the dielectric tensor of stable β-Ga_2O_3[26] and the ordinary dielectric function of ε-Ga_2O_3,[27] but lower than that of corundum α-Ga_2O_3.[28] The tiny contribution to ε_2 at ≈4.6eV is most likely an artifact due to an imperfect model description of the sample. From $\varepsilon_1(\hbar\omega \to 0)$, the dielectric limit of the material, usually referred to as ε_∞, can be estimated to be 3.9 ± 0.1.

Figure 6a shows a response- and substrate-corrected PLE map of γ-Ga_2O_3 at 5 K. It is dominated by a strong and broad excitation channel centered around 5.33 eV feeding a broad luminescence with an intensity maximum at 3.17 eV. The corresponding excitation spectra for selected temperatures between 5 and 300 K are displayed in Figure 6b. The maxima of PLE intensity (dots) shift to lower excitation energies starting at around 150 K. This shift can be well approximated by phenomenological expressions commonly used to describe the temperature dependence of bandgaps in semiconductors,[29,30] as shown by the solid line in Figure 6c. The derived values for the high-temperature slope of 3.2(9) meV K^{-1} and the low temperature energy gap $E(T = 0) =$ 5.330(3) eV do not vary significantly depending on the specific

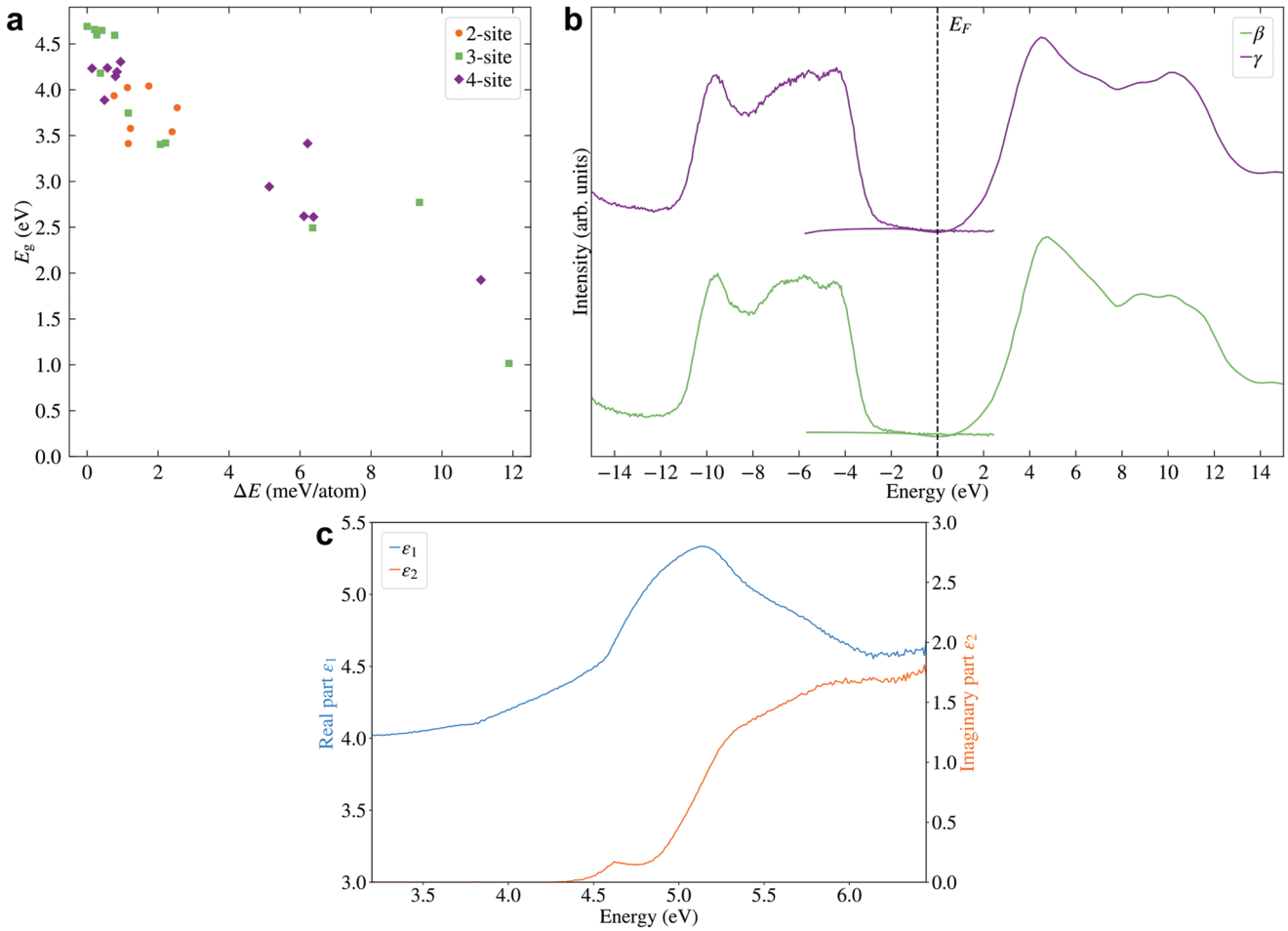

Figure 5. Bandgap and band alignment of γ-Ga_2O_3. a) Relative energy, ΔE versus bandgap, E_g for all relaxed structures, where both quantities have been calculated using HSE. b) Soft X-ray photoelectron spectra of the valence band states and O X-ray absorption spectra of the conduction states of both γ- and β-Ga_2O_3 plotted on a common energy axis.[24] c) Point-by-point fitted dielectric function of γ-Ga_2O_3 in the visible and ultraviolet spectral range.

model chosen (ref. [29]) was used here). At room temperature the PLE maximum is observed at 5.17 eV, thus downshifted by 160 meV compared to $T = 0$ K, which indicates that the highest excitation efficiency coincides with the onset of strong absorption (5.1 eV) observed in spectroscopic ellipsometry (Figure 5c). It should be noted that the PLE spectrum is not generally expected to be identical to the corresponding absorption spectrum as only absorptive processes that lead to the occupation of electronic states which participate in the emission of the detected luminescence contribute to the PLE signal. In the present case, this can be observed in the high energy region ($E > 5.5$ eV), where the PLE signal decreases (Figure 6b) despite increasing absorption (Figure 5c), implying that at higher energies different relaxation paths become available that do not contribute to the measured luminescence band. The bandgap values from spectroscopic ellipsometry and room temperature PLE are in good agreement with each other and somewhat larger than the SXPS/XAS and HSE predicted values, pointing toward a mismatch of electronic and optical bandgaps. It is worth noting that this effect appears more pronounced for γ-Ga_2O_3, as calculations with the same methods yield good agreement with experiment for other polymorphs, such as the β and α phases.[24,26,31,32] One potential explanation may be due to localization effects in the uppermost valence band states, which we describe in more detail below and in the Supporting Information.

In order to explore the electronic structure of the occupied states in more detail, projected density of states (PDOS) calculations of the 30 relaxed structures were performed (see Figures S6 and S7, Supporting Information for PDOS results of select structures). After broadening and photoionization cross section weighting, the PDOS can be directly compared to the experimental SXPS and HAXPES valence spectra (see **Figure 7**a,e, respectively). As is the case of the other Ga_2O_3 polymorphs, the valence band (VB) of the γ phase is dominated by O 2p states with small contributions from Ga 3d and 4s states at the top and bottom of the VB. The influence of photoionization cross sections is obvious when comparing the SXPS and HAXPES spectra in these figures, in particular the decrease of the O p state contribution when going to higher X-ray energies. The cross section effects are useful in identifying the individual orbital contributions to the overall valence band as well as validating the theoretically predicted PDOS.

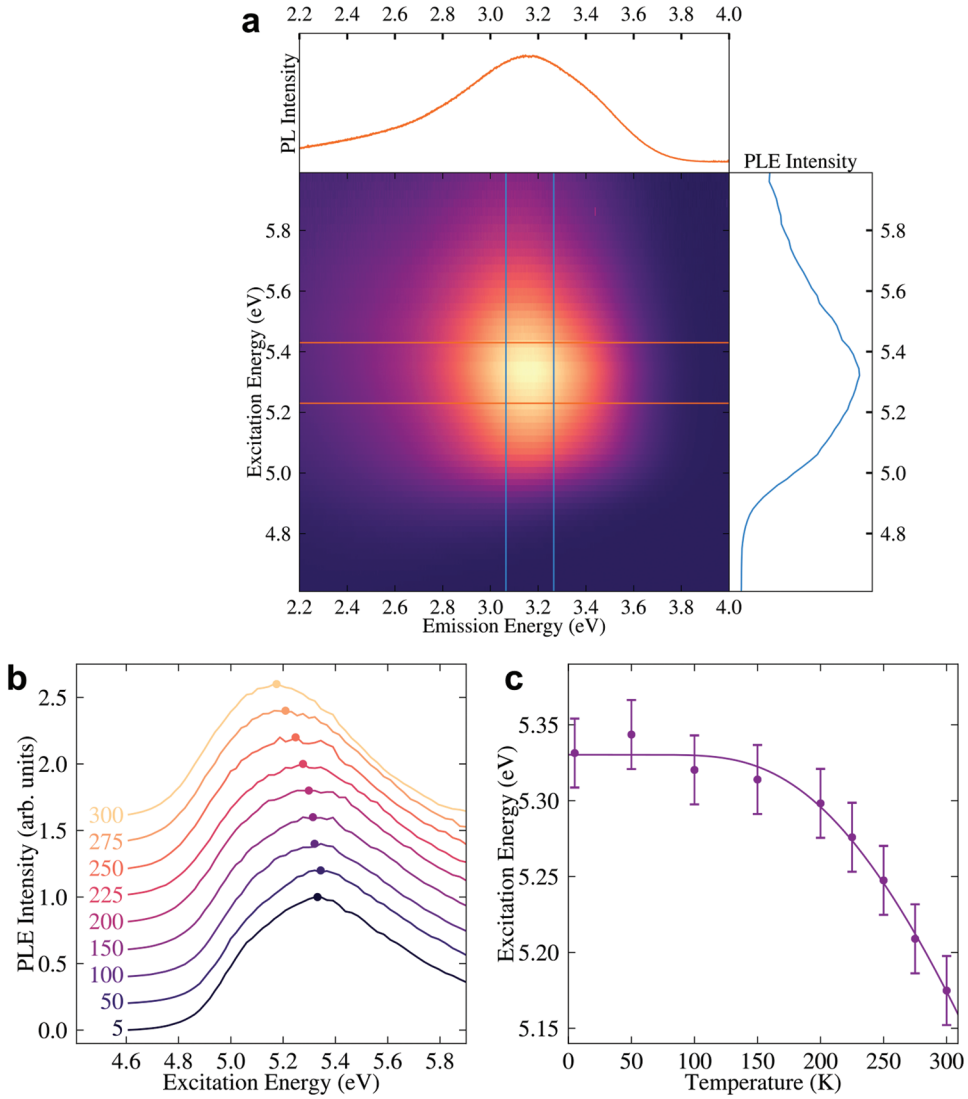

Figure 6. PLE spectra of γ-Ga_2O_3. a) 2D map of excitation energy as function of emission energy as obtained by PLE measurement of the γ-Ga_2O_3 film at a temperature of 5 K. The top and right graphs display corresponding PL and PLE spectra as obtained within ±100 meV energy intervals around the intensity maxima of 3.17 and 5.33 eV, respectively. b) Integrated PLE spectra as a function of temperature between 5 and 300 K. The spectra have been normalized and shifted vertically for clarity. The dots mark approximate excitation energy corresponding to highest PLE signal. c) Energy of the excitation maximum in the PLE spectra as function of temperature between 5 and 300 K (dots and corresponding error bars). The solid line represents a semi-empirical fit of the temperature dependence of the excitation energy.[29,30]

Whilst good agreement is found with the photoelectron spectra for the overall valence band, significant localization of the highest-lying valence band states of γ-Ga_2O_3 is found, while no such localization was observed in the conduction band states. Localization extends to ≈0.8 eV below the highest occupied state for the lowest energy structure, as can be seen in Figures S8 and S9, Supporting Information. Preliminary analysis of the calculated optical transitions (Figure S8, Supporting Information) indicate weaker transition strengths between the more localized valence band states and the conduction band, as compared to the more delocalized states at higher transition energies. This behavior in the model γ-Ga_2O_3 structures is similar to that observed in other semiconducting amorphous oxides,[33] and may account for the discrepancy between the measured optical and electronic bandgaps.

Overall good agreement is found between the PDOS of the low energy structures (ΔE < 10 meV per atom) and the PES results. The 3- and 4-site structures are almost indistinguishable in their PDOS, with the 2-site structures showing some differences. Variations in PDOS increase when moving to the medium energy structures (10 ≤ ΔE < 20 meV per atom), while the high energy structures (ΔE ≥ 20 meV per atom) start to vary extensively, deviating clearly from the experimental spectra. In addition, in the predicted high energy structures, in-gap states start to appear, which are clearly not present in the experimental data of the γ-Ga_2O_3 samples. Therefore, whilst PES cannot distinguish between the lowest energy structures as the differences predicted from theory are too subtle to be identified in the experimental data, it demonstrably shows that the higher energy structures are not a realistic description of γ-Ga_2O_3.

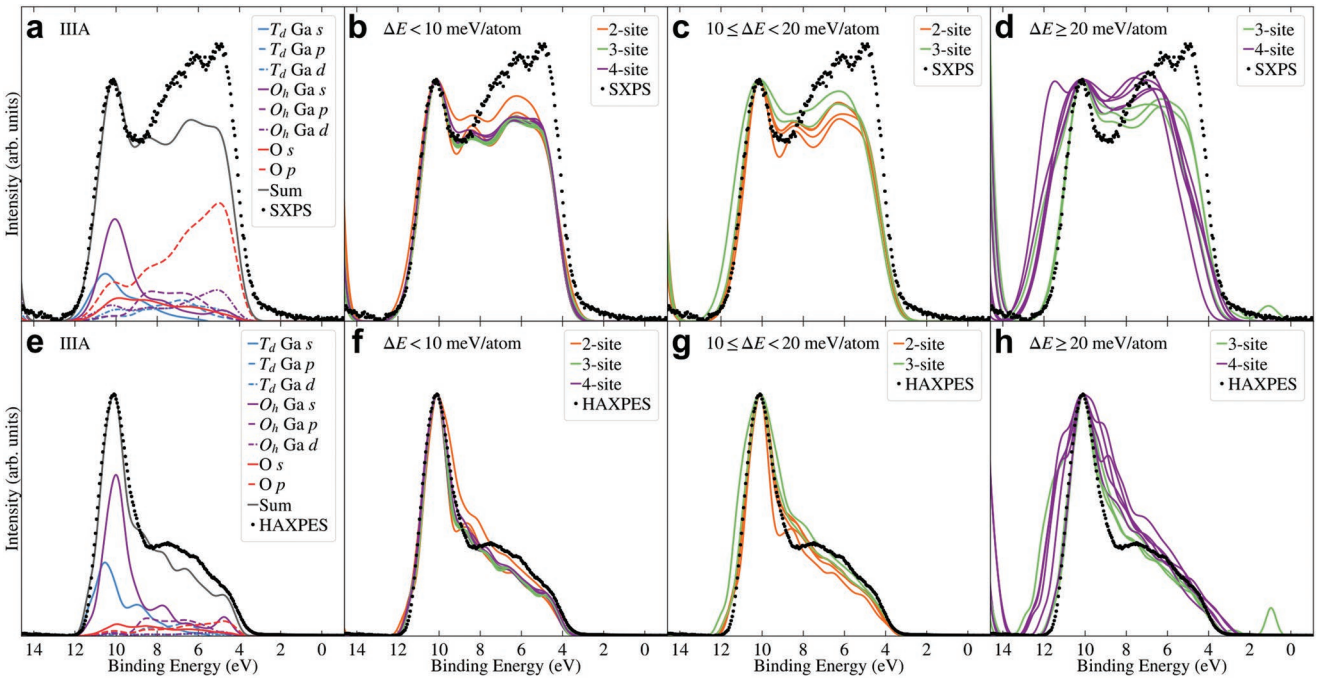

Figure 7. a–h) Comparison between the calculated and measured valence XPS for soft (a–d) and hard (e–h) X-rays. The theoretical results are for the 30 relaxed structures listed in Table S2, Supporting Information grouped by energy relative to the lowest energy relaxed structure. (a) and (e) show the weighted PDOS for the lowest energy structure for the SXPS and HAXPES case, respectively. The theoretical spectra have been aligned and normalzed to the peak dominated by Ga s states at the bottom of the VB.

2.5. Semicore Spectra

Semicore (shallow core) states can have a significant influence on the final electronic structure of metal oxide semiconductors. **Figure 8** shows the theoretical spectra from PBE and HSE calculations, as well as the experimental SXPS spectra of the semicore states and the valence band, with the calculated spectra coming from the lowest energy structure. HSE shows an improvement in the agreement between its predicted semicore energies and SXPS as compared to PBE, while still showing disagreement of several eV relative to the experimental peak positions of the highest binding energy (BE) states in Figure 8. This is expected from these levels of theory, which suffer from different amounts of self-interaction errors that impact the calculated bandgap, and the p–d-repulsion that influences the BE positions of semicore levels and valence band states. In addition, theory underestimates the level of hybridization in Ga_2O_3, leading to differences in relative peak intensities of the semicore states and different relative errors for the O- and Ga-derived semicore levels. This leads to a typical underestimation of the semicore levels with respect to experiment, which can be improved with higher levels of theory such as those that treat many-body interactions like the GW approximation.[24] Nevertheless, their overall shape and orbital character is described well even with PBE, as will be discussed in the following.

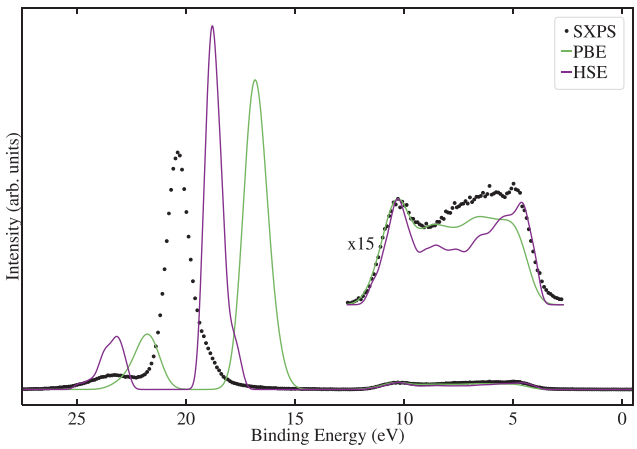

Figure 8. Comparison of the weighted occupied PDOS from both PBE and HSE for the lowest energy structure with the experimental SXPS results, including both the valence bands and semicore states. The theoretical spectra are aligned to the dominant Ga s feature at the bottom of the valence band. The detailed PDOS from both PBE and HSE can be found in Figure S10, Supporting Information.

The semicore states in Ga_2O_3 show two peaks of O 2s and Ga 3d character, for which the broadened and cross section corrected PDOS for the lowest energy γ-Ga_2O_3 structure, as well as the SXPS and HAXPES data, are shown in **Figure 9**a,e. Following the arguments presented for the valence spectra above, combining SXPS and HAXPES can help to identify the orbital character of observed spectral features and verify theoretical projections. The dominant feature in the semicore spectra is the predominantly Ga 3d peak (at 21.1 eV in the SXPS data), with contributions from T_d and O_h sites reflecting the ratio of sites present within the structure, with O_h dominating. In addition, a shoulder toward the lower BE of the main feature is due to hybridization with O 2s states. The difference in the

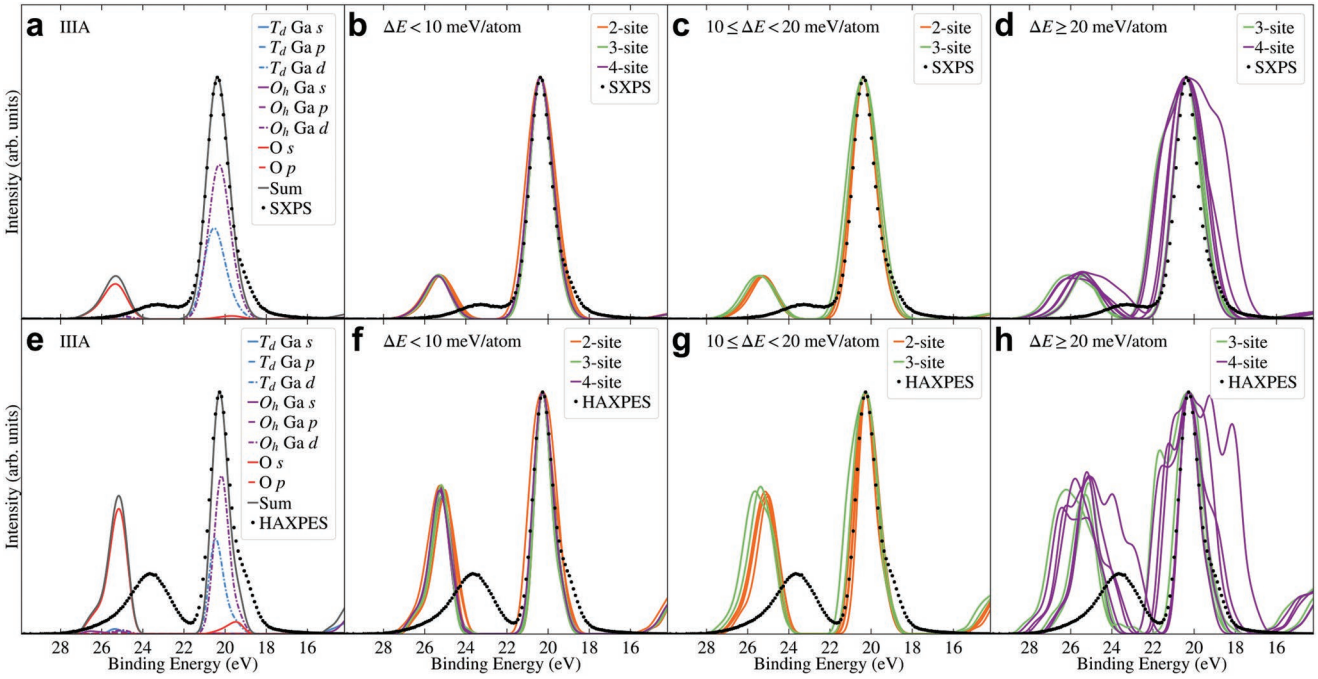

Figure 9. Comparison between calculated and measured semicore states for SXPS and HAXPES. a,e) The weighted PDOS for the lowest energy structure (3-site structure) for SXPS and HAXPES, respectively. b–d,f–h) Theoretical results for the 30 relaxed structures listed in Table S2, Supporting Information grouped by energy relative to the lowest energy relaxed structure, and compared to the experimental SXPS and HAXPES spectra, respectively. The theoretical spectra are aligned and normalized to the peak with the maximum height.

decay in photoionization cross sections between O 2s and Ga 3d, with the O 2s cross section decreasing at a slower rate compared to the Ga 3d one, leads to this shoulder being more pronounced in the HAXPES spectra compared to the SXPS spectra. This clear cross sectional dependence is also obvious in the second semicore state (at 24.5 eV in the HAXPES data), which is largely dominated by O 2s states and which changes considerably in relative intensity when going from soft to hard X-rays.

Figure 9b–d,f–h show the comparison of the experimental spectra with the calculated spectra for the 30 relaxed structures listed in Table S2, Supporting Information, grouped by energy relative to the lowest energy relaxed structure, for SXPS and HAXPES, respectively. Unweighted PDOS and comparison between the calculated and measured semicore XPS for soft and hard X-rays for select relaxed structures can be found in Figures S11 and S12, Supporting Information. Whilst only very minimal differences exist between the lowest energy (<10 meV per atom) structures, changes become more obvious for structures with energies $10 \leq \Delta E < 20$ meV per atom, particularly in the HAXPES case due to the discussed relative increase in the O 2s cross section. Finally, for the high energy structures with $\Delta E \leq 20$ meV per atom, the calculated spectra no longer resemble the experiment. The resulting width increase, in particular for the Ga 3d dominated feature, originates from the spreading in energies for both Ga and O states, which is magnified due to hybridization in the semicore states. As was evident from VB spectra, the higher energy structures are not a realistic representation of γ-Ga_2O_3.

2.6. Core-Level Spectra

Although core-level spectra are often overlooked as a source of information regarding the relationship between local coordination and electronic structure of a material, recent work has shown that the full width at half maximum (FWHM) of core-levels, in particular of O 1s, can change significantly depending on local coordination environments in Ga_2O_3 polymorphs.[24] Ga $2p_{3/2}$ and O 1s core-level spectra of γ-Ga_2O_3, as well as β-Ga_2O_3 for comparison, were collected using both SXPS and HAXPES and are shown in **Figure 10**. The advantage of collecting core-level spectra with both SXPS and HAXPES is that any surface related effects affecting SXPS data, such as hydroxylation, undercoordination, and band bending, do not influence the HAXPES spectra considerably. This is due to the considerable increase in probing depth upon the increase in X-ray energy and therefore kinetic energy of the photoelectrons. The Ga $2p_{3/2}$ spectra are near identical in SXPS and HAXPES except for the small difference in the energy resolution of the two measurements. The O 1s spectra also have comparable FWHM and line shapes in SXPS and HAXPES, with the SXPS data showing a small shoulder on the higher BE side of the main photoionization peak due to surface species, such as hydroxyl groups. The surface-related features are not included in the theoretical calculations as these are based on a bulk description of γ-Ga_2O_3, resulting in a closer match with the HAXPES data compared to the SXPS data.

The FWHM of the HAXPES core-level spectra are almost identical at 1.15±0.01 eV for O 1s and 1.29 ± 0.01 eV for Ga $2p_{3/2}$ for both γ and β-Ga_2O_3. To understand this observation, core

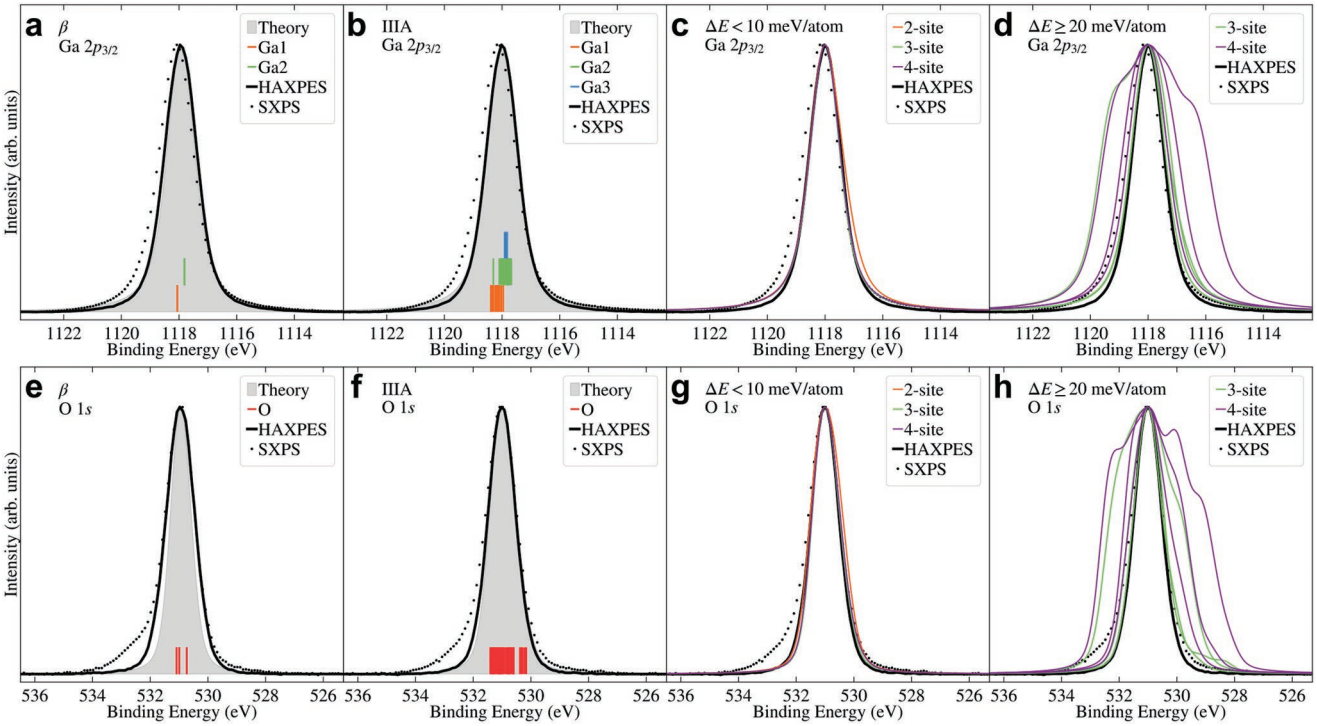

Figure 10. Comparison between the calculated and measured core states for Ga $2p_{3/2}$ (top) and O 1s (bottom), for both SXPS and HAXPES. a,b,e,f) The different site contributions for the lowest energy γ-Ga_2O_3 structure (b,f) (equivalent plots for the other structures are shown in Figure S11, Supporting Information), and the reference results for β-Ga_2O_3 (a,e). c,d,g,h) The theoretical results for the lowest 2-, 3-, and 4-site relaxed structures, as well as the six highest energy (3- and 4-site) relaxed structures. Calculations are grouped by energy relative to the lowest energy relaxed structure. The theoretical spectra are normalized and aligned with respect to experiment.

BE calculations were performed and the results are shown in Figure 10b,f for the lowest energy γ and (a) and (e) for the reference β structure. In the much simpler β case, two clearly separated contributions (with a difference in energy ΔE of 0.25 eV) from T_d Ga1 and O_h Ga2 to the Ga $2p_{3/2}$ core level are found. In contrast, the relative energies in the γ case are spread out due to the differences in coordination environment, with a maximum difference in energy ΔE_{max} = 0.71 eV. O 1s shows similar behavior albeit with an in general larger ΔE_{max} (0.36 eV in β-Ga_2O_3) and also a greater magnitude of spreading in the γ structure (to ΔE_{max} = 1.25 eV). This heightened sensitivity of O 1s to changes in local coordination compared to Ga $2p_{3/2}$ is in agreement with previous observations on Ga_2O_3 polymorphs.[24]

Due to the high computational cost of core BE calculations (where each atom in the cell requires a separate DFT calculation), core BEs were only calculated for nine structures: the lowest energy relaxed 2-, 3-, and 4-site structures, and the six highest energy relaxed structures. Since there are no high energy relaxed 2-site structures, this comprised three 3-site and three 4-site structures. Figure 10c,g show the comparison of the experimental spectra to calculated spectra for the lowest energy structures with two, three and four occupied Ga sites. Similar to the observations made for the semicore states, it is clear that only very minimal differences exist between these structures, which are too small to influence the overall line profile of the experimental core-level spectra. In contrast, the spectra from the highest energy structures shown in Figure 10d,h show various levels of deviation, including some extreme cases for the 4-site structures, where there is a much larger spread of BE values for both Ga $2p_{3/2}$ and O 1s. This is common to all Ga sites, as shown in Figure S13 and Table S3, Supporting Information. A possible explanation for this greater spread of values comes from the rough trend that the higher the energy of the structure, the greater the number of distinct environments present in the unrelaxed structure, as depicted in Figure S14, Supporting Information. In addition, the in some cases extreme broadening of BE is due to the appearance of unrealistic environments in these structures. Although the higher energy structures in particular change significantly during relaxation, it is nonetheless likely that they typically retain a greater diversity in local environment, leading to the wider spread of BE values.

3. Conclusion

The present work showcases a successful strategy for theoretically screening and experimentally validating potential atomic structures of the disordered material γ-Ga_2O_3 and assessing their relationship to its electronic structure. By combining the screening of nearly a million structures with more than a thousand DFT calculations, a number of low energy candidate structures were successfully identified. Based on the developed robust atomistic model, bandgaps, densities of states, as well as semi core and core state energies were calculated and directly compared to experimental efforts across a range of advanced techniques. The results convincingly show that the predicted

low energy structures are a suitable representation of disorder in γ-Ga_2O_3, whilst predicted higher energy structures result in dramatic deviations from experiments. Of the low energy structures, both 3- and 4-site models provide good descriptions of the experimental data, with 2-site models showing worse agreement. This work opens up pathways to more extensive theoretical explorations of this material, such as going beyond fixed lattice parameters and treating larger supercells, to enable a more realistic treatment of long range disorder. Furthermore, the complementarity between theoretical and experimental approaches demonstrated here shows the potential for applying such a strategy to many other disordered systems where, whilst technologically interesting, structure—electronic structure relations have been challenging (or impossible) to explore.

4. Experimental Section

Structure Generation: Atomic structures were generated using the structure of Playford et al.,[9] using a fixed lattice constant of 8.2376 Å. Preliminary calculations in smaller cells showed a strong sensitivity to stoichiometry, therefore all calculations were performed in a stoichiometric $1 \times 1 \times 3$ supercell (160 atoms). The Ga sites were randomly occupied, first by selecting a site with a probability such that each type of Ga site was selected with the same frequency. The selected site was then occupied using the following probabilities. For 10% of the 800 initial $1 \times 1 \times 3$ structures only the first two sites (Ga1 and Ga2) were occupied, with equal probability. For the remainder of the structures, all four Ga sites were randomly occupied, with probabilities of 0.741, 0.741, 0.066, and 0.024 for Ga1 through Ga4, respectively, following ref. [9]. To avoid unphysically short Ga–Ga distances, a minimum Ga–Ga distance of 2.4 Å was imposed. Due to the combination of the distance constraint and randomized approach, even in the case where all four sites had a nonzero probability, many structures nonetheless had only two or three sites occupied, as summarized in Table S1, Supporting Information.

DFT Calculations: Except where stated otherwise, DFT calculations were performed using the semi-local PBE functional.[34] Single point energy calculations and geometry optimizations employed the wavelet-based BigDFT code,[35] using HGH-GTH pseudopotentials (PSPs),[36,37] also including non-linear core corrections for O.[38] The Ga PSP included three valence electrons, with the 3d electrons treated as part of the core. Calculations used a wavelet grid spacing of 0.38 bohr and coarse (fine) radius multipliers of 5 (7), and were performed at the Γ-point only. In order to aid convergence for screening calculations, and since a number of the generated structures were found to have a negligible bandgap, density mixing was used with a finite temperature of 0.001 Ha. Structures which did not converge within 500 diagonalization iterations (≈2% of initial structures) were discarded. Geometry optimizations were performed using a direct minimization approach without finite temperature, since a bandgap opened up during relaxation for all structures. A maximum force threshold of 0.03 eV $Å^{-1}$ was employed, while the unit cell was kept fixed.

PDOS calculations were performed using the CASTEP plane-wave DFT code,[39] employing a kinetic energy cut-off of 700 eV. Ultrasoft PSPs were employed with the Ga 3d electrons treated as valence states. The density was obtained at the Γ-point only, while the PDOS was calculated on a $2 \times 2 \times 1$ Monkhorst–Pack *k*-point grid.[40] Post-processing was performed using OptaDOS,[41] with 0.44 eV (0.25 eV) Gaussian smearing applied for comparison with soft (hard) X-rays to reflect the experimental broadening. To further aid comparison of theory and experiment, Scofield photoionization cross sections for the experimental soft and hard X-ray energies were applied to the calculated PDOS using Galore.[42–44] Unweighted PDOS were broadened using 0.44 eV Gaussian smearing.

Relative core BE were also calculated with CASTEP, using the ΔSCF approach, in which a core hole was introduced into the excited atom by means of an on-the-fly generated core hole PSP. Core-hole calculations were then performed with a net charge. For Ga, the core-hole PSP was generated using an averaged approach, that is, the electron was not removed from a specific p-orbital, and thus the calculated BEs did not specifically correspond to the $2p_{3/2}$ states. The same cut-off energy and PSPs were employed as for PDOS calculations. Due to the higher computational cost of core BE calculations, which require one calculation per atom in a given structure, calculations were only performed for select structures, at the Γ-point only. Core BE and PDOS calculations were also performed for β-Ga_2O_3, using the same PSPs and cut-off energy, and an $8 \times 8 \times 8$ Monkhorst–Pack *k*-point grid. The unit cell was taken from ref. [45]. The structure was relaxed using CASTEP using a maximum force threshold of 0.03 eV $Å^{-1}$ while keeping the cell fixed, otherwise using the same parameters as the core BE calculations. BEs were calculated for each atom in the cell, regardless of whether they are equivalent by symmetry. For both γ and β phases, the spectra were generated by applying a combination of 0.25 eV Gaussian smearing to reflect the experimental broadening of the HAXPES data and 0.38 eV (0.133 eV) Lorentzian smearing for Ga (O) to reflect the different intrinsic line widths of the Ga and O lines.

To evaluate the bandgaps beyond semilocal functionals, HSE06 screened hybrid functional calculations were employed. These calculations were performed with the VASP code with 32% mixing of exact exchange, a 400 eV plane-wave cut-off and PAW potentials that include the Ga 3d states as valence electrons, which had been previously shown to accurately describe the properties of β-Ga_2O_3.[24] All atomic coordinates in the 160-atom model γ-Ga_2O_3 structures were allowed to relax and the direct bandgap was evaluated at the zone-center with a Γ-centered *k*-point mesh including Γ and another *k*-point at the zone boundary at 0.5,0.5,0.5. Owing to the size of the supercells, this bandgap may also include contributions from higher-lying valence band states that were folded to the Γ-point in the supercells. For the lowest energy structure, the density of states was further resolved with a 5× 5 ×1 Γ-centered mesh. This larger *k*-point sampling confirmed the indirect bandgap nature of γ-Ga_2O_3, with the indirect valence band maximum (VBM) falling at least 0.05 eV higher than the highest-lying valence band state at the Γ-point of the supercell.

Machine-Learning Approach: Since the number of possible structures is too large for an exhaustive search, a machine-learning (ML) approach was implemented to nonetheless enable the screening of a large number of structures. The employed model relied on the decomposition of a structure into a set of distinct (reference) local atomic environments. Each reference environment, α had an associated energy, ε_α, with the total energy of a given structure, *E*, defined as

$$E = \sum_{\alpha=1}^{N_{\text{env}}} M_\alpha \varepsilon_\alpha \tag{1}$$

where M_α is the number of instances of α in the structure and N_{env} is the total number of reference environments. The decomposition of the total energy into local atomic energies was well established in the ML community, and had been employed with a range of descriptors.[46,47] In this work, a simple descriptor based only on the local coordination environment was used, as described below.

For each atom *i* of species s in a given structure, all Ga (O) atoms within a radius of r_c^{s-Ga} (r_c^{s-O}) of atom *i* were identified. Atom *i* and these neighboring atoms constitute environment α. Given another environment β, centered on atom *j* of the same species *s*, the two environments may be said to be equivalent if both α and β contained the same number of Ga and O atoms, that ia, if $N_\alpha^{Ga} = N_\beta^{Ga}$ and $N_\alpha^{O} = N_\beta^{O}$. Otherwise, the two environments were treated as distinct. In other words, only the number of atoms of each species present within the environment was taken into consideration, irrespective of their actual atomic coordinates. Since all O sites were fully occupied, all O–O interactions were excluded, that is, $r_c^{O-O} = 0.0$ Å. Therefore, the approach relied on only two parameters: r_c^{Ga-Ga} and $r_c^{Ga-O} \equiv r_c^{O-Ga}$.

The decomposition of a given atomic structure then proceeds as follows, as illustrated in Figure S15, Supporting Information. For each

atom i in the input structure, its local environment α was obtained, given user-defined cut-off radii. Environment α was then compared to each of the existing reference environments β associated with an atom of the same species as atom i. If none of the existing environments were equivalent to α, then α was a new, distinct environment and was added to the set of reference environments. The process was repeated for each atom in the structure, and again for subsequent structures, taking the already existing set of reference structures as an input, adding new reference environments as needed.

Once all structures within a given data set had been decomposed into a set of reference environments, the data was split into training and validation sets, where each structure which contained a previously unseen reference environment must be included in the training set. The energies of each environment, ε_α, were then obtained by fitting to DFT-calculated energies using ridge regression, as implemented in Scikit-learn.[48] In order to determine the cut-off distances, r_c, single point calculations were performed for 800 initial structures. The structures were split randomly into 534 (226) training (validation) structures. To account for variations due to the choice of training set, five randomized splits were tested. The model was then fit using different values of r_c, which were chosen so as to include increasing shells of neighbors, as depicted in Figure S16, Supporting Information. For each pair of r_c values, the regularization parameter was varied between 0.5 and 50 in intervals of 0.5. For each case, the value giving the lowest MAE of the validation set, when averaged across the five splits, was then employed. As shown in Table S4, Supporting Information, the values $r_c^{Ga-Ga} = 4.3$ Å and $r_c^{Ga-O} = 4.8$ Å gave the lowest MAE and are therefore used in the following.

Having established the model hyperparameters, a number of additional structures were generated using the four site occupancies, in order to improve the coverage of the data set. A DFT calculation was then performed for each structure which contained either new (i.e., not already encountered) reference environments, or rare reference environments, which were present in less than five structures. The structures were generated in batches of 20 000, discarding unconverged structures following the same criterion as before. The process was repeated until a total of 400 000 additional structures had been generated, giving rise to an extra 39 converged structures. Although such an approach did not guarantee that all possible environments were represented, it was assumed that any remaining unrepresented environments were either very rare, or only occur in structures which did not converge, and were thus likely to be high in energy and therefore ultimately unfavorable. The model was then refit by splitting the data into 560 (279) training (validation) structures. The regularization value, α, was again varied as described above; a final value of 0.5 was employed.

Growth and Structure: An epitaxial γ-Ga_2O_3 film was grown on a double polished (001) $MgAl_2O_4$ substrate using conventional plasma-assisted molecular beam epitaxy (MBE), which was used for all photoelectron and optical experiments. Beam fluxes of Ga and O radicals were supplied to the heated substrate from an effusion cell and an RF-radical cell, respectively. The nominal Ga flux measured in vacuum was 2.2×10^{-8} Torr and an input RF power of 200 W and an oxygen flow rate of 0.50 standard cubic centimeters per minute (sccm) were used to generate oxygen radicals for the growth. In the oxygen background during growth, the Ga effusion cell mainly provided Ga_2O at a higher flux than the pure Ga flux provided during the beam-flux measurement in vacuum.[49] The substrate temperature was 600 °C with a total growth time of 2000 s. The film thickness as estimated from the growth rate (2.8 nm min^{-1}) was 92 nm. The surface roughness as determined from atomic force microscopy was 0.8 nm. Further details can be found in previous publications.[50–52]

The crystal phase of the produced epitaxial film was investigated using X-ray diffraction (XRD). Data collection was performed on a high-resolution X-ray diffractometer (Rigaku SmartLab) using monochromated Cu Kα_1 radiation. The strong $MgAl_2O_4$ 001 substrate reflection was observed at 44.8° with the γ-Ga_2O_3 004 film reflection at lower 2θ (42.6°) indicating successful epitaxial stabilization (see Figure S17, Supporting Information). The FWHM of the 004 rocking curve was 0.4°.

In addition, γ-Ga_2O_3 films were grown by solid-phase epitaxy on c-plane Al_2O_3 substrates for the TEM experiments. For this purpose, an amorphous Ga_2O_3 film was grown by plasma-assisted MBE on a 2″ c-plane Al_2O_3 substrates at a substrate temperature of 125 °C, a Ga flux of 2×10^{-7} mbar (corresponding to a Ga_2O_3 growth rate of 3.6 nm min^{-1}), and an oxygen flux of 3 sccm at an RF plasma power of 300 W. The growth time of 35 min resulted in an estimated film thickness of ≈120 nm. Within the first 20 s of growth (i.e., the first 1.2 nm), the spotty reflection high-energy electron diffraction patterns (RHEED) pattern of the substrate changed into a featureless, diffused one, indicating the formation of an amorphous film. After growth, the substrate was split into smaller pieces for the subsequent crystallization of the amorphous film.

The amorphous films were annealed in an oven under O_2 at atmospheric pressure isochronal for 30 min increasing the temperature from 400 to 900 °C in steps of 100 °C. The structure of the samples was analyzed by X-ray diffraction in a Bragg–Brentano geometry with -2θ scans after each annealing step. Figure S18, Supporting Information shows the XRD ω–2θ scans of as grown amorphous Ga_2O_3 thin films on sapphire substrate after annealing at the various temperatures. The sample annealed at 400 °C showed exclusively $(0003)_n$ reflections of the sapphire substrate indicating the sample still to be amorphous within the detection limit of X-ray diffraction. After further annealing to 500 °C, additional reflections were revealed (indexed with a, b, c, and d). These peaks can be assigned $(111)_n$ reflections of the γ-phase $(111)_n$, and they were close in position to the $(20\overline{1})_n$ reflections of the β phase. The XRD data showed that peaks (a) and (c) match literature data of the (201) and (603) reflections of the β phase increasing in intensity with increasing temperature. Peaks (b) and (c) decreased in intensity with increasing temperature and shift to nominal values that corresponded to reflections of the γ phase. These observations were commensurate with a gradual transition from the γ-phase to the β-phase at higher temperatures. The sample annealed at 500 °C was used for the high resolution transmission electron microscopy experiments presented.

X-ray Photoelectron and Absorption Spectroscopy: γ-Ga_2O_3 samples were investigated using both soft (SXPS) and hard (HAXPES) X-ray photoelectron spectroscopy. Laboratory-based SXPS was performed on a Thermo Scientific K-Alpha+ spectrometer with a monochromated microfocused Al Kα X-ray source ($h\nu$ = 1486.7 eV) and a spot size of 400 µm. The base pressure of the instrument was 2×10^{-9} mbar and the X-ray source was operated at 6 mA emission current and 12 kV anode bias. Pass energies of 20 eV for core level and 15 eV for valence band spectra were used. HAXPES data were collected at beamline I09 at Diamond Light Source, UK, at a photon energy of 5.9403 keV.[53] A double-crystal Si (111) monochromator was combined with a Si (004) channel-cut crystal as a post-monochromator to achieve the final energy resolution. The main end station at beamline I09 was equipped with a VG Scienta EW4000 electron analyzer, which had a wide acceptance angle of ±28°. All measurements were performed in grazing incidence geometry at angles below 5° between the incoming X-ray beam and the sample surface and a pass energy of 200 eV was used for all spectra. The resolution of SXPS and HAXPES measurements, as determined by the width of the Fermi edge of gold, are 0.44 and 0.25 eV, respectively. The HAXPES valence band spectrum was also collected at beamline P22 at PETRA III/DESY to confirm the reproducibility under varying beamline conditions.[54] The I09 and P22 spectra were identical and information on the experimental setup at P22, as well as a comparative plot of the data, can be found in Figure S19, Supporting Information. The β-Ga_2O_3 core-level reference spectra were collected on a (010) oriented bulk single crystal obtained from Novel Crystal Technology Inc., Tamura Corporation. The semicore and core spectra for γ- and β-Ga_2O_3 shown in Figures 9 and 10 are all aligned to the O 1s core level of the SXPS experiments. Beamline I09 was also used to collect XAS of the O K-edge in total electron yield mode and details on the alignment procedure can be found in a previous publication.[24]

Spectroscopic Ellipsometry: Spectroscopic ellipsometry was performed using a scanning variable-angle spectroscopic ellipsometer based on a grating monochromator operational in the spectral range between 0.5 and 6.5 eV. The instrument was equipped with an autoretarder. The γ-Ga_2O_3 film was measured using three different angles of incidence Φ of 50°, 60°, and 70°. The recorded experimental ellipsometric parameters Ψ and Δ were analyzed using a multilayer model to find the complex dielectric function as a function of photon energy $\varepsilon(\hbar\omega)$. For the present case, the model consisted of the substrate $MgAl_2O_4$, the γ-Ga_2O_3 layer of interest, and an effective medium approximated surface roughness layer using the Bruggeman formalism.[55] Layer thicknesses were found to be 122 nm (γ-Ga_2O_3) and 3.3 nm (effective medium layer). The dielectric function of $MgAl_2O_4$ has already been determined by Zollner et al.[56] Their results were compared and slightly modified to match the identical (001) $MgAl_2O_4$ crystal, which was used as a substrate in the present study. For the description of the γ-Ga_2O_3 layer, a model independent so-called point-by-point fitted dielectric function was obtained by fitting the calculated optical response of the multilayer model to the experimental ellipsometric parameters while varying the real and imaginary parts of $\varepsilon(\hbar\omega) = \varepsilon_1(\hbar\omega) + i\varepsilon_2(\hbar\omega)$ until best agreement was obtained. The cubic crystal structure of γ-Ga_2O_3 had an isotropic optical response, this means the dielectric function was a scalar for this material.

PLE Spectroscopy: PLE was performed using a 400 W Xe arc lamp, which was monochromatized by a two-stage spectrometer (Acton SP250, f = 250 mm, gratings: 1800 lines mm^{-1}) yielding a spectral FWHM of the excitation beam of around 1 nm. The samples were placed in a He-flow microcryostat (Janis ST-500) enabling temperature-dependent measurements between 5 and 300 K. The optical excitation and detection of the emitted light was performed in backscattering geometry using a UV fused silica beamsplitter and focusing lens (NA = 0.69). The emitted light was dispersed in a single-stage monochromator (Acton SP300, 300 mm, grating: 300 lines mm^{-1}) and detected by a charge-coupled device (Horiba Syncerity). Reference measurements of the $MgAl_2O_4$ substrate were conducted alongside the PLE measurements of the γ-Ga_2O_3 thin film under equal conditions to correct for the non-negligible substrate signal in overlapping spectral regions. The PLE spectra were corrected to account for the spectral power density of the lamp and transmission losses throughout the optical setup by in situ monitoring of the excitation light using a UV-optimized high sensitivity Si photodiode (Hamamatsu S4349). The excitation spectra were obtained by integrating over the full width of the detected luminescence signal and were proportional to the probability that an exciting photon generated an emitted photon in the observed emission wavelength range.

Supporting Information

Supporting Information is available from the Wiley Online Library or from the author.

Acknowledgements

L.E.R. acknowledges support from an EPSRC Early Career Research Fellowship (EP/P033253/1) and the Thomas Young Center under grant number TYC-101. Calculations were performed on the Imperial College High Performance Computing Service and the ARCHER UK National Supercomputing Service. The authors are also grateful to the UK Materials and Molecular Modelling Hub for computational resources, which is partially funded by EPSRC (EP/P020194/1 and EP/T022213/1). Work by F.N., E.K., R.G., M.F., P.M., O.B., C.W., M.N., M.A., and M.R.W. was performed in the framework of GraFOx, a Leibniz-ScienceCampus partially funded by the Leibniz association. M.R.W. and B.M.J. acknowledge funding by the German Research Foundation DFG (project number 446185170). J.E.N.S. acknowledges funding through the Engineering and Physical Sciences Research Council (EPSRC) Center for Doctoral Training in New and Sustainable Photovoltaics (EP/L01551X/1). C.K. acknowledges the support from the Department of Chemistry at University College London. A.R. acknowledges the support from the Analytical Chemistry Trust Fund for her CAMS-UK Fellowship. The authors acknowledge Diamond Light Source for time on Beamline I09 under Proposals SI21430-1 and SI24670-1. The authors would like to thank Dave McCue, I09 beamline technician, for his support of the experiments. The authors acknowledge DESY (Hamburg, Germany), a member of the Helmholtz Association HGF, for the provision of experimental facilities. Parts of this research were carried out at PETRA III, beamline P22. Beamtime was allocated for proposal H-20010087. The work by J.B.V. was partially performed under the auspices of the U.S. DOE by Lawrence Livermore National Laboratory under contract DE-AC52-07NA27344, and partially supported by LLNL LDRD funding under project number 22-SI-003 and by the Critical Materials Institute, an Energy Innovation Hub funded by the U.S. DOE, Office of Energy Efficiency and Renewable Energy, Advanced Manufacturing Office. Figures 1a and 4a were prepared using the VESTA software package.[57]

Conflict of Interest

The authors declare no conflict of interest.

Data Availability Statement

The data that support the findings of this study are openly available in GitLab at https://gitlab.com/lratcliff/gamma-ga2o3, project ID 29286257.

Keywords

electronic structure, gallium oxide, machine learning, photoluminescence excitation spectroscopy, semiconductors, structural disorder, ultrawide bandgap

Received: May 10, 2022
Revised: July 5, 2022
Published online:

[1] S. J. Pearton, J. Yang, P. H. Cary, F. Ren, J. Kim, M. J. Tadjer, M. A. Mastro, *Appl. Phys. Rev.* **2018**, *5*, 011301.
[2] J. Shi, J. Zhang, L. Yang, M. Qu, D.-C. Qi, K. H. L. Zhang, *Adv. Mater.* **2021**, *33*, 2006230.
[3] D. Guo, Q. Guo, Z. Chen, Z. Wu, P. Li, W. Tang, *Mater. Today Phys.* **2019**, *11*, 100157.
[4] Y. Teng, L. X. Song, A. Ponchel, Z. K. Yang, J. Xia, *Adv. Mater.* **2014**, *26*, 6238.
[5] X. Hou, Y. Zou, M. Ding, Y. Qin, Z. Zhang, H. Sun, S. Long, *J. Phys. D: Appl. Phys.* **2021**, *54*, 043001.
[6] M. Akatsuka, Y. Kawaguchi, R. Itoh, A. Ozawa, M. Yamamoto, T. Tanabe, T. Yoshida, *Appl. Catal. B* **2020**, *262*, 118247.
[7] H. Masataka, S. Kohei, M. Hisashi, K. Yoshinao, K. Akinori, K. Akito, M. Takekazu, Y. Shigenobu, *Semicond. Sci. Technol.* **2016**, *31*, 34001.
[8] H. W. Xue, Q. M. He, G. Z. Jian, S. B. Long, T. Pang, M. Liu, *Nanoscale Res. Lett.* **2018**, *13*, 290.
[9] H. Y. Playford, A. C. Hannon, E. R. Barney, R. I. Walton, *Chem. Eur. J.* **2013**, *19*, 2803.
[10] J. Böhm, *Angew. Chem.* **1940**, *53*, 131.

[11] R. Roy, V. G. Hill, E. Osborn, *J. Am. Chem. Soc.* **1952**, *74*, 719.
[12] K. Pohl, *Naturwissenschaften* **1968**, *55*, 82.
[13] H. Y. Playford, A. C. Hannon, M. G. Tucker, D. M. Dawson, S. E. Ashbrook, R. J. Kastiban, J. Sloan, R. I. Walton, *J. Phys. Chem. C* **2014**, *118*, 16188.
[14] P. Hohenberg, W. Kohn, *Phys. Rev.* **1964**, *136*, B864.
[15] W. Kohn, L. J. Sham, *Phys. Rev.* **1965**, *140*, A1133.
[16] S. Yoshioka, H. Hayashi, A. Kuwabara, F. Oba, K. Matsunaga, I. Tanaka, *J. Phys.: Condens. Matter* **2007**, *19*, 346211.
[17] H. Hayashi, R. Huang, F. Oba, T. Hirayama, I. Tanaka, *Appl. Phys. Lett.* **2012**, *101*, 241906.
[18] G. Gutiérrez, A. Taga, B. Johansson, *Phys. Rev. B* **2001**, *65*, 012101.
[19] H. P. Pinto, R. M. Nieminen, S. D. Elliott, *Phys. Rev. B* **2004**, *70*, 125402.
[20] T. Taniike, M. Tada, Y. Morikawa, T. Sasaki, Y. Iwasawa, *J. Phys. Chem. B* **2006**, *110*, 4929.
[21] X. Wang, M. Faizan, G. Na, X. He, Y. H. Fu, L. Zhang, *Adv. Electron. Mater.* **2020**, *6*, 2000119.
[22] R. Meng, M. Houssa, K. Iordanidou, G. Pourtois, V. Afanasiev, A. Stesmans, *J. Appl. Phys.* **2020**, *128*, 034304.
[23] G. Paglia, A. L. Rohl, C. E. Buckley, J. D. Gale, *Phys. Rev. B* **2005**, *71*, 224115.
[24] J. E. N. Swallow, C. Vorwerk, P. Mazzolini, P. Vogt, O. Bierwagen, A. Karg, M. Eickhoff, J. Schörmann, M. R. Wagner, J. W. Roberts, P. R. Chalker, M. J. Smiles, P. Murgatroyd, S. A. Razek, Z. W. Lebens-Higgins, L. F. J. Piper, L. A. H. Jones, P. K. Thakur, T.-L. Lee, J. B. Varley, J. Furthmüller, C. Draxl, T. D. Veal, A. Regoutz, *Chem. Mater.* **2020**, *32*, 8460.
[25] J. B. Varley, J. R. Weber, A. Janotti, C. G. Van de Walle, *Appl. Phys. Lett.* **2010**, *97*, 142106.
[26] C. Sturm, J. Furthmüller, F. Bechstedt, R. Schmidt-Grund, M. Grundmann, *APL Mater.* **2015**, *3*, 106106.
[27] E. Kluth, P. Ning, J. Grümbel, A. Karg, M. Eickhoff, R. Goldhahn, M. Feneberg, unpublished.
[28] M. Feneberg, J. Nixdorf, M. Neumann, N. Esser, L. Artús, R. Cuscó, T. Yamaguchi, R. Goldhahn, *Phys. Rev. Mater.* **2018**, *2*, 044601.
[29] K. O'Donnell, X. Chen, *Appl. Phys. Lett.* **1991**, *58*, 2924.
[30] R. Pässler, *Phys. Status Solidi B* **1997**, *200*, 155.
[31] J. Furthmüller, F. Bechstedt, *Phys. Rev. B* **2016**, *93*, 115204.
[32] F. Bechstedt, J. Furthmüller, *Appl. Phys. Lett.* **2019**, *114*, 122101.
[33] M. Kim, I. J. Kang, C. H. Park, *Curr. Appl. Phys.* **2012**, *12*, S25.
[34] J. P. Perdew, K. Burke, M. Ernzerhof, *Phys. Rev. Lett.* **1996**, *77*, 3865.
[35] L. E. Ratcliff, W. Dawson, G. Fisicaro, D. Caliste, S. Mohr, A. Degomme, B. Videau, V. Cristiglio, M. Stella, M. D'Alessandro, S. Goedecker, T. Nakajima, T. Deutsch, L. Genovese, *J. Chem. Phys.* **2020**, *152*, 194110.
[36] S. Goedecker, M. Teter, J. Hutter, *Phys. Rev. B* **1996**, *54*, 1703.
[37] C. Hartwigsen, S. Goedecker, J. Hutter, *Phys. Rev. B* **1998**, *58*, 3641.
[38] A. Willand, Y. O. Kvashnin, L. Genovese, Á. Vázquez-Mayagoitia, A. K. Deb, A. Sadeghi, T. Deutsch, S. Goedecker, *J. Chem. Phys.* **2013**, *138*, 104109.
[39] S. J. Clark, M. D. Segall, C. J. Pickard, P. J. Hasnip, M. I. Probert, K. Refson, M. C. Payne, *Z. Kristall.* **2005**, *220*, 567.
[40] H. J. Monkhorst, J. D. Pack, *Phys. Rev. B* **1976**, *13*, 5188.
[41] A. J. Morris, R. J. Nicholls, C. J. Pickard, J. R. Yates, *Comput. Phys. Commun.* **2014**, *185*, 1477.
[42] J. H. Scofield, Theoretical Photoionization Cross Sections from 1 to 1500 keV, Technical report, U.S. Atomic Energy Commission, Divison of Technical Information Extension, **1973**, https://www.osti.gov/biblio/4545040/ (accessed: May 2022).
[43] C. Kalha, N. K. Fernando, A. Regoutz, Digitisation of Scofield Photoionisation Cross Section tabulated data **2020**, https://figshare.com/articles/dataset/Digitisation_of_Scofield_Photoionisation_Cross_Section_Tabulated_Data/12967079 (accessed: May 2022).
[44] A. J. Jackson, A. M. Ganose, A. Regoutz, R. G. Egdell, D. O. Scanlon, *J. Open Source Softw.* **2018**, *3*, 773.
[45] J. Åhman, G. Svensson, J. Albertsson, *Acta Cryst. C* **1996**, *52*, 1336.
[46] F. Musil, A. Grisafi, A. P. Bartók, C. Ortner, G. Csányi, M. Ceriotti, *Chem. Rev.* **2021**, *121*, 9759.
[47] J. A. Keith, V. Vassilev-Galindo, B. Cheng, S. Chmiela, M. Gastegger, K.-R. Müller, A. Tkatchenko, *Chem. Rev.* **2021**, *121*, 9816.
[48] F. Pedregosa, G. Varoquaux, A. Gramfort, V. Michel, B. Thirion, O. Grisel, M. Blondel, P. Prettenhofer, R. Weiss, V. Dubourg, J. Vanderplas, A. Passos, D. Cournapeau, M. Brucher, M. Perrot, E. Duchesnay, *J. Mach. Learn. Res.* **2011**, *12*, 2825.
[49] G. Hoffmann, Z. Cheng, O. Brandt, O. Bierwagen, *APL Mater.* **2021**, *9*, 111110.
[50] T. Oshima, Y. Kato, M. Oda, T. Hitora, M. Kasu, *Appl. Phys. Express* **2017**, *10*, 051104.
[51] T. Oshima, Y. Kato, E. Magome, E. Kobayashi, K. Takahashi, *Japanese J. Appl. Phys.* **2019**, *58*, 060910.
[52] Y. Kato, M. Imura, Y. Nakayama, M. Takeguchi, T. Oshima, *Appl. Phys. Express* **2019**, *12*, 065503.
[53] T.-L. Lee, D. A. Duncan, *Synchrotron Radiat. News* **2018**, *31*, 16.
[54] C. Schlueter, A. Gloskovskii, K. Ederer, I. Schostak, S. Piec, I. Sarkar, Y. Matveyev, P. Lömker, M. Sing, R. Claessen, C. Wiemann, C. M. Schneider, K. Medjanik, G. Schönhense, P. Amann, A. Nilsson, W. Drube, *AIP Conf. Proc.* **2019**, *2054*, 040010.
[55] D. A. G. Bruggeman, *Ann. Phys.* **1935**, *24*, 636.
[56] C. J. Zollner, T. I. Willett-Gies, S. Zollner, S. Cho, *Thin Solid Films* **2014**, *571*, 689.
[57] K. Momma, F. Izumi, *J. Appl. Crystallogr.* **2011**, *44*, 1272.